



Ultrasensitive DNA biosensor for hepatitis B virus detection based on tin-doped WO₃/In₂O₃ heterojunction nanowire photoelectrode under laser amplification

Mohsen Shariati¹ · Mahdi Sadeghi¹

Received: 9 April 2020 / Revised: 10 May 2020 / Accepted: 2 June 2020 / Published online: 13 June 2020
© Springer-Verlag GmbH Germany, part of Springer Nature 2020

Abstract

The fabrication of a highly sensitive DNA biosensor based on tin-doped WO₃/In₂O₃ nanowires as heterojunction photoelectrode for detection of hepatitis B virus is reported. The tin-doped WO₃/In₂O₃ nanowires were fabricated via a physical vapor deposition mechanism and were nearly 50 nm in width. The single-strand DNA probe was covalently immobilized on the nanowire surface. The biosensor could detect the hybridization of complementary DNA in a label-free approach at very low concentrations. The biodetection processes were conducted through reduction-oxidation reactions in the electrochemical impedance spectral measurements. The electrochemical impedance responses were biased under laser amplification to achieve the detection limit of 1 fM. The fabricated biosensor could detect DNA concentrations from 0.1 pM to 10 μM linearly in the calibration plot. Due to laser amplification, more charged carriers were released and they interacted with DNA on the electrode surface. The efficiency of the charge transfer parameter was enhanced by a photogeneration process, and the electron-hole recombination rate could intensively increase biosensor sensitivity, selectivity, and distinguishability. The stability of the nanowire biosensor under laser amplification demonstrated 96% of its initial responses after 6 weeks of maintenance.

Keywords Label-free DNA biosensor · Hepatitis B virus · WO₃/ITO nanowires · Laser amplification · Electrochemical impedance

Introduction

Identification of sequences which are specific to human nucleic acids has been widely recognized as an important diagnosis technique in identifying diseases [1]. Today, the cause of many human hereditary disorders related to genetic mutation has been identified, and this knowledge is steadily expanding with the sequencing of the human genome [2]. Recently, viruses have been shown responsible for diseases that are recognizable by their nucleic acid sequences [3]. Hepatitis B is a liver viral infection and can chronically spread

the infection [4]. Today, hepatitis B infection is a global biological problem that affects the public health of people around the world [5]. Liver cancer and liver failure are among the most common problems for people with hepatitis B virus (HBV) infection [6]. The virus's transmission is mainly through human blood [7]. Therefore, the necessity of virus detection at an early stage is one of the developed programs of medical identification. In recent years based on the virus DNA function, various methods for HBV detection have been employed such as detection based on optical [8], transistor [9], and electrochemical [10] sensors. An enzymatic method has also been used recently to detect the DNA of the virus [11].

The electrochemical impedance spectra (EIS) diagnostic technique is one of the most obliged methods for the DNA hybridization detection in label-free biosensors [12, 13]. In order to measure the dielectric parameters of a biosystem, the EIS technique could be used in a wide frequency range and different potentials [13–16]. Recently, the EIS has been able to analyze and study significant parameters such as adsorption on the surface, transport of electric carriers, ionic diffusion, and ion migration [13–17]. The electrode and

Electronic supplementary material The online version of this article (<https://doi.org/10.1007/s00216-020-02752-z>) contains supplementary material, which is available to authorized users.

✉ Mohsen Shariati
shariatimohsen59@gmail.com

¹ Medical Physics Department, School of Medicine, Iran University of Medical Science, Tehran 14155-6183, Iran

electrolyte interface which is the source of basic electrochemical developments has been fundamentally discussed and investigated by the EIS technique [13–15]. For studying the cell culture, antibody/antigen interactions, and hybridization of DNA sequences, the EIS as a non-destructive biosystem detective has shown the promising results [18–22]. Recently, membranes have been employed as the key component for the nanoporous impedance biosensors [13–18]. Although the application of polycarbonate structures has resolved the problems in DNA hybridization sensing such as probe immobilization and target hybridization on the surface [14–18], the main challenge for membranes is that the high surface area requires high concentrations of the DNA strands [17]. In order to overcome the problem of using the high concentration, novel solutions by means of deposition of nanostructures in porous and non-porous platforms have been proposed [14–17]. The nanostructured materials such as nanowires (NWs) have been widely used in impedance-based biosensors for diagnostic purposes of the biosystems [23–25]. The NWs were able to detect DNA in label-free approach at very low concentrations [22–24].

In this paper, an impedimetric biosensor for HBV DNA detection under laser amplification based on tin-doped $\text{WO}_3/\text{In}_2\text{O}_3$ nanowire ($\text{WO}_3/\text{indium tin oxide (ITO) NW}$) photoelectrode has been materialized. The materialized WO_3/ITO NWs with well-controlled thickness have been used as the base electrode for biosensing. The charge transfer measurements were conducted for investigating the DNA immobilization and hybridization via the EIS quantification. The WO_3/ITO NW electrode under laser enhanced the surface coverage, detection sensitivity, and selectivity of the biosensor. By optimizing the biosensor performance under laser stimulation, WO_3/ITO NW electrode showed high sensitivity.

Materials and experiments

Materials

The indium, tin, and tungsten metals (99.999% purity) were purchased from Sigma-Aldrich Co. (USA). The quartz substrates were purchased from Sina Corp. (Iran). The DNA immobilization and hybridization buffers were Tris-EDTA (TE) buffer (10 mM Tris HCl, 1 mM EDTA, pH 7.2) and 2× saline sodium citrate (SSC; 300 mM NaCl, 20 mM $\text{Na}_3\text{C}_6\text{H}_5\text{O}_7$, pH 7.0), respectively. The aqueous 2 mM $\text{K}_3\text{Fe}(\text{CN})_6/\text{K}_4\text{Fe}(\text{CN})_6$ with supporting electrolyte (0.2 M KCl) which was prepared in deionized water (DIW) was involved in the EIS measurement cell. The sequences of DNA oligonucleotide (25-mer sequences) probe, complementary, non-complementary, and mismatch targets with HPLC purification were purchased from Bioneer Co. (South Korea). The sequences of oligonucleotides were evaluated with Basic Local Alignment

Search Tool (BLAST). The DNA solutions were prepared with sterile distilled (SD) water and maintained at a freezer at $-25\text{ }^\circ\text{C}$. The sequences of DNA oligonucleotides are listed in Table 1.

Preparation of $\text{WO}_3/\text{In}_2\text{O}_3$ NW arrays

In order to fabricate WO_3/ITO NWs, the physical vapor deposition (PVD) growth mechanism was applied to materialize the self-assembled indium thin film. The heat treatment process associated with annealing was conducted in a tubular furnace. The (In + Sn 10:1) metal precursor was used to grow the alloyed structure. The metal precursor was 0.3 mm in size and positioned in alumina boat. All precursor metals were in 99.999% purity, and the final weight was 0.3 g. Some pre-preparation paces such as sonication in acetone bath and gas-drying for substrate cleansing were applied. In first step for NW growth materialization, the epitaxial formation of the indium thin film on substrates was conducted. The epitaxial growth process under vacuum was performed by the PVD mechanism. In second step, tin and then indium were evaporated on the film for creating sandwich platform (indium (In) + tin (Sn) + indium (In)). After thin film fabrication step, the samples were put in furnace. Finally, tungsten metal was put in the furnace and exposed to oxygen and argon gas. The controlled pressure was fixed at 10^{-4} mbar. The furnace temperature was kept around $1500\text{ }^\circ\text{C}$. In order to characterize the fabricated NWs, several investigations were conducted by instrumental analyses. The X-ray diffraction (XRD) pattern measurement was conducted for NW phase characterization. The morphological and lattice structure investigations were performed by field emission scanning electron microscopy (FESEM) and high-resolution transmission electron microscopy (HRTEM). An X-ray diffractometer was used to map the XRD pattern measurements (40 kV, $\text{CuK}\alpha$). A Hitachi S-4160 FESEM microscope was applied for NW morphology characterization. A HRTEM microscope (Philips, CM-30) was used to investigate the morphology, sizes, and growth directions of the NWs (HRTEM and SAED patterns). For laser amplification, a 300-W Xe-arc lamp light source (PerkinElmer PE300BUV) was applied under controlled conditions. Figure 1 shows the schematic illustration of the electrochemical cell under laser amplification.

DNA immobilization and hybridization process on the WO_3/ITO NW surface

For immobilizing the single-strand DNA (ssDNA) probe on the WO_3/ITO NW surface, the ssDNA oligonucleotides, firstly, were immersed in 0.1 M dithiothreitol (DTT) solution for 25 min to break the disulfide bond of the thiolated oligonucleotides. Then, the DNA probe in $1\text{ }\mu\text{M}$ concentration ($1\text{ }\mu\text{L}$) was immersed in TE buffer and was drop-casted on the

Table 1 DNA materials

Sequence name	Sequence of oligonucleotides	Company (country)
Thiolated probe	5'-HS (CH ₂) ₆ TAC CGT CCC CTT CTT CAT CTG CCG T-3'	Bioneer Corporation (South Korea)
Target	5'-ACG GCA GAT GAA GAA GGG GAC GGT A-3'	Bioneer Corporation (South Korea)
1-point mismatch	5'-ACG CCA GAT GAA GAA GAA GAC GGT A-3'	Bioneer Corporation (South Korea)
Non-complementary	5'-TAC CGT CCC CTT CTT CAT CTG CCG T-3'	Bioneer Corporation (South Korea)

electrode surface. Finally, the electrode was kept in the box for hindering the contamination. The electrode was preserved for 8 h and then washed with DIW. It should be noted that the surface of the NWs, due to gold coating for electron microscopic analysis, made it possible to immobilize the thiolated oligonucleotides. Therefore, the connection of the electrode surface to thiolated DNA was done by covalent bonding.

In order to hybridize the probe with the target oligonucleotides, 1 μL of complementary oligonucleotides with concentrations from 0.1 pM to 1 μM in SSC buffer was introduced to the WO₃/ITO NWs and the electrode was kept in the box for hindering the contamination. Finally, the samples were rinsed by SSC and the impedance tests were implemented.

Electrochemical measurements

The EIS measurements were performed by a potentiostat (Autolab PG STAT302N potentiostat instrumented with the frequency response analyzer (FRA32) module; Metrohm Autolab Co., Netherlands) associated with a conventional electrochemical cell in three-electrode system, Ag/AgCl as reference, platinum as counter, and WO₃/ITO NWs as working electrode. For drawing the Nyquist plots, the Teplot 360 software (Teplot, Inc., USA) with computational fluid

dynamics (CFD) formats was applied. The EIS measurements were conducted in the 0.01–100 kHz frequency range, and the perturbation potential was + 10 mV. The measurements were performed in OCP conditions related to bias voltage. In order to optimize the properties of the HBV DNA biosensor for amplifying the signal-to-noise responses, the laser stimulated the WO₃/ITO NW photoelectrode with the beam energy equal to WO₃/ITO NW band gap. The mathematical surface area of NW electrode was 1 cm². All the EIS measurements were conducted 3 times.

Results and discussion

Morphological and elemental characterization

Figure 2 shows the FESEM pictures of the materialized NWs. It certainly is observable that the electrode is composed of a large quantity of NWs on quartz support substrate. They are in typical lengths beyond a few hundreds microns and around 50–70 nm in diameter. Figure 2 shows the grown NWs in 1-D nano-growth process. The tin-doped In₂O₃ played as a catalyst and substantiated the catalyst-mediated vapor-liquid-solid growth process in 1-D nanofabrication. It could be estimated that the tin-doped In₂O₃ role was to form the final shapes and rightly modulate the lateral side to raise uniform, homogeneous, and metrological shapes.

Figure 3 shows the TEM and HRTEM images of tin-doped WO₃/In₂O₃ NWs from the selected sample with a dimension of ~50 nm diameter in which their corresponding HRTEM image is demonstrated in inset. The HRTEM image indicates that the WO₃/ITO NWs is tremendously crystalline. However, the tin and indium doping in hybrid manner effectively helps the growth of NWs. The HRTEM image truly establishes the morphology of the ITO-WO₃ NWs. The two interplane interspaces were studied, and the lattice planes could be indexed to (200) for NW with [040] for the growth-orientated direction (see Fig. 3). The lattice spacing for selected NW is 0.518 nm. The mentioned lattice spacing of NW is consistent to (200) planes. These crystal planes are coinciding with the WO₃/ITO phase structure. The growth direction which is coinciding with the past articles was recognized to be [040] for NW [23].

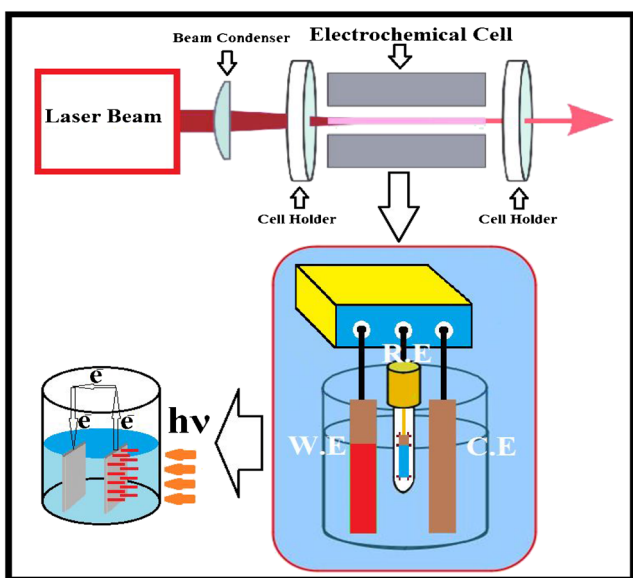


Fig. 1 Schematic image of WO₃/ITO NW electrode under laser radiation

Fig. 2 The FESEM pictures of fabricated samples. (a) Scale = 10 μm . (b) Scale = 4 μm

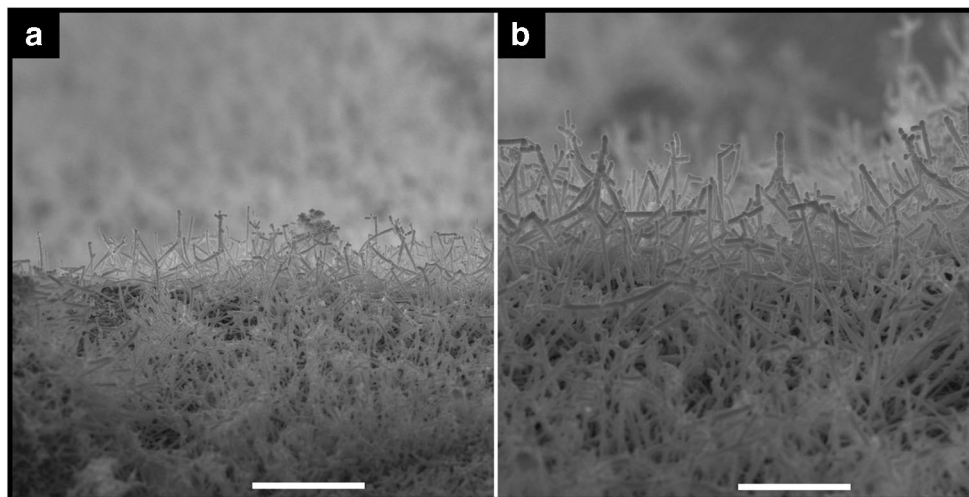


Figure S1 (see the Electronic Supplementary Material (ESM)) illustrates the XRD patterns of the grown NWs. The room-temperature XRD pattern was performed to measure the lattice phase of the fabricated NWs and growth directions. The XRD spectrum was obtained from tin-doped In_2O_3 -based WO_3 NWs at room temperature. The crystalline phases of WO_3 /ITO NWs were validated. The XRD measurement demonstrates the WO_3 main peak indexes which should be related to the monoclinic phase in unit cell parameters $a = 0.7297$ nm, $b = 0.7539$ nm, $c = 0.7688$ nm, and $\beta = 90.91^\circ$ corresponding to the JCPDS (43-1035); however, the XRD pattern has peaks indexed greatly to the body-centered cubic (bcc) In_2O_3 phase with the calculated cell parameter $a = 10.12$ \AA , (JCPDS file no. 6-0416) [22, 23]. No impurity phases were detected in the XRD pattern, and the strong peaks conferred the NW crystallinity.

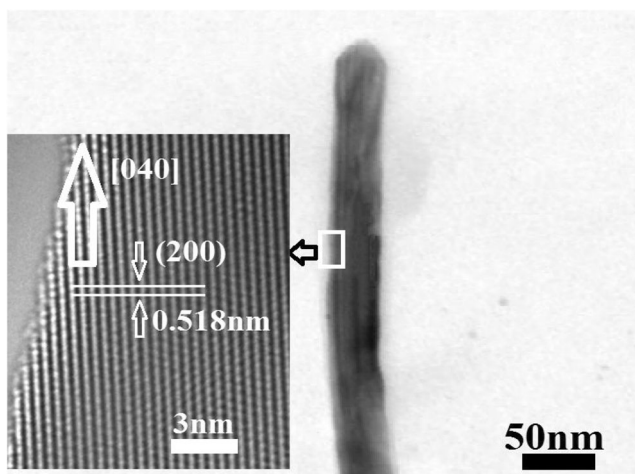


Fig. 3 The bright-field TEM image of the NW. Inset, HRTEM image of the selected area with lattice spacing and growth direction

Growth mechanism

In this study, the used method provided the necessary parameters for the growth of NWs. The annealing process was recognized as an important key process to obtain satisfactory results. One of the important steps in the process of the NW materialization is the nucleation stage. In the PVD mechanism, the nucleation step would be rarely and hardly accomplished, and in this way, fewer NWs can be fabricated. It needs to be said that oxygen gas seriously was able to conduct the nucleation site materialization. These nucleation sites were crucial for the direct growth of NWs. The oxidation process occurred during the nucleation stage and reduced the problems associated with NW growth on the substrate surface [22, 23].

Figure 4 shows the schematic picture of the NW growth process. The applied technique resulted to the NW synthesis with interesting morphology. Laterally, the thinnest dimension of the NWs is about 50 nm (Fig. 2). The WO_3 /ITO NWs were found to nucleate from indium tin oxide-based nanoclusters. The lateral dimension of the NWs precisely was controlled by indium tin alloy in ITO crystallization step. As a result, the lateral dimensions of the NWs were thinner in comparison to previous observed experiments [23]. The two factors played the main roles for the growth of the tin-doped In_2O_3 -based WO_3 NWs: first, the nucleated seeding on the substrate, and second, the doping material. The heat treatment associated with the annealing process in the presence of carrier and oxidation gas caused the formation of nanoparticles (NPs) which materialized the oriented and unidirectional growth of the NWs. The surface of the nanostructured sites and clusters adsorbed the NPs by reducing the free energy which caused the NWs to grow. As the annealing temperature decreased, both the morphological shape and the dimension of the NWs were disrupted. The annealing temperature caused the lateral

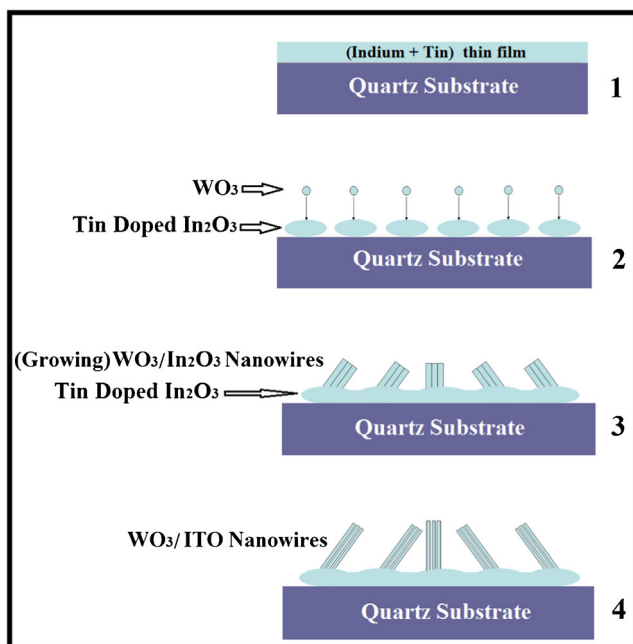


Fig. 4 The schematic picture of WO₃/ITO NW growth. Step 1, double layer thin film. Step 2, nucleation and site fabrication in the presence of vapor. Step 3, NW growth. Step 4, continuous growth

dimension formation and improved the NW growth distribution on the seeded surface [23].

For investigating the DNA probe immobilization on the NW surface, the fluorescein-modified probe oligonucleotides were immobilized and fluorescence illustrations were clearly visualized. First, the NWs were put in the highly sensitive electronic aligner. This electronic aligner could effect on the free charges on the NW surface and conducted the NW and DNA alignment in the electric field direction. After immersing the electrode surface in phosphate-buffered saline (PBS) and acetone solutions associating with thermal accommodation, the NW electrode was cleansed with purified DIW. Fluorescein-modified oligonucleotides were immobilized on the unmodified and functional surface. The functionalization of the NW surface could facilitate the fluorescence image materialization. The immobilization of large amounts of DNA probe oligonucleotides was confirmed by the high-intensity fluorescence (Fig. 5). In Fig. 5, the obvious fluorescence quantity contrast between the functional and unadapted sites is visible. Because of the materialization effects on the NW surface, the blue and violet backgrounds in the fluorescence imaging were observed.

The electrochemical biosensor

The analytical EIS measurements for biosensor before laser amplification

Selectivity The selectivity of the DNA biosensor after hybridization of the probe with mismatch, non-complementary, and

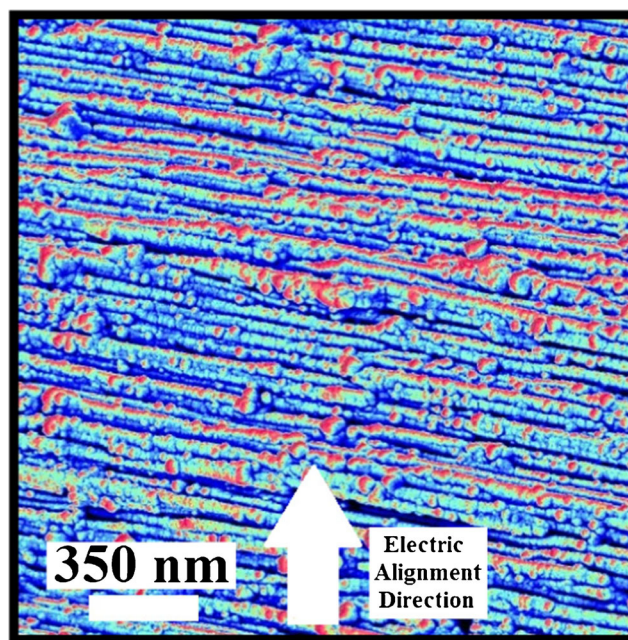


Fig. 5 The fluorescein-modified probe oligonucleotide immobilization and fluorescence illustration

complementary oligonucleotides was investigated. Figure 6a shows the selectivity of the WO₃/ITO NW surface with DNA probe, mismatch, non-complementary, and complementary targets in 1 μ M concentration. In Fig. 6a, the EIS Nyquist plots were investigated for the WO₃/ITO NW electrode modified with probe and targets. The decreased electrostatic interactions between the redox couples and the WO₃/ITO NW surface (repulsive interactions) are the main factors that significantly impact the R_{ct} changes. The electrostatic repulsion prevented the charge transfer in the interface [13–20]. The WO₃/ITO NW probe-modified electrode showed the lowest R_{ct} . In Fig. 6a, the results indicated that the WO₃/ITO NW-modified electrode has a significant ability for DNA sensing. The corresponding R_{ct} values were decreased from 2487 to 806 Ω for DNA complementary target and probe, respectively. In other means, the charge transfer was hindered after probe hybridization with complementary target sequences, R_{ct} was increased, and the resistance change was $\Delta R_{ct} = 1681 \Omega$. Because of electrostatic and steric repulsion, the probe electrode showed the intensive charge transfer between electrolyte and the electrode surface. The semicircle diameter was reduced by charge transfer enchantment [2–4]. The semicircle diameter value of the non-complementary DNA in comparison to DNA probe was enhanced. Because of the electrostatic repulsive interactions between the redox elements and WO₃/ITO NWs, the EIS measurements for non-complementary target in comparison to mismatch target showed more charge transfer and decreased resistance.

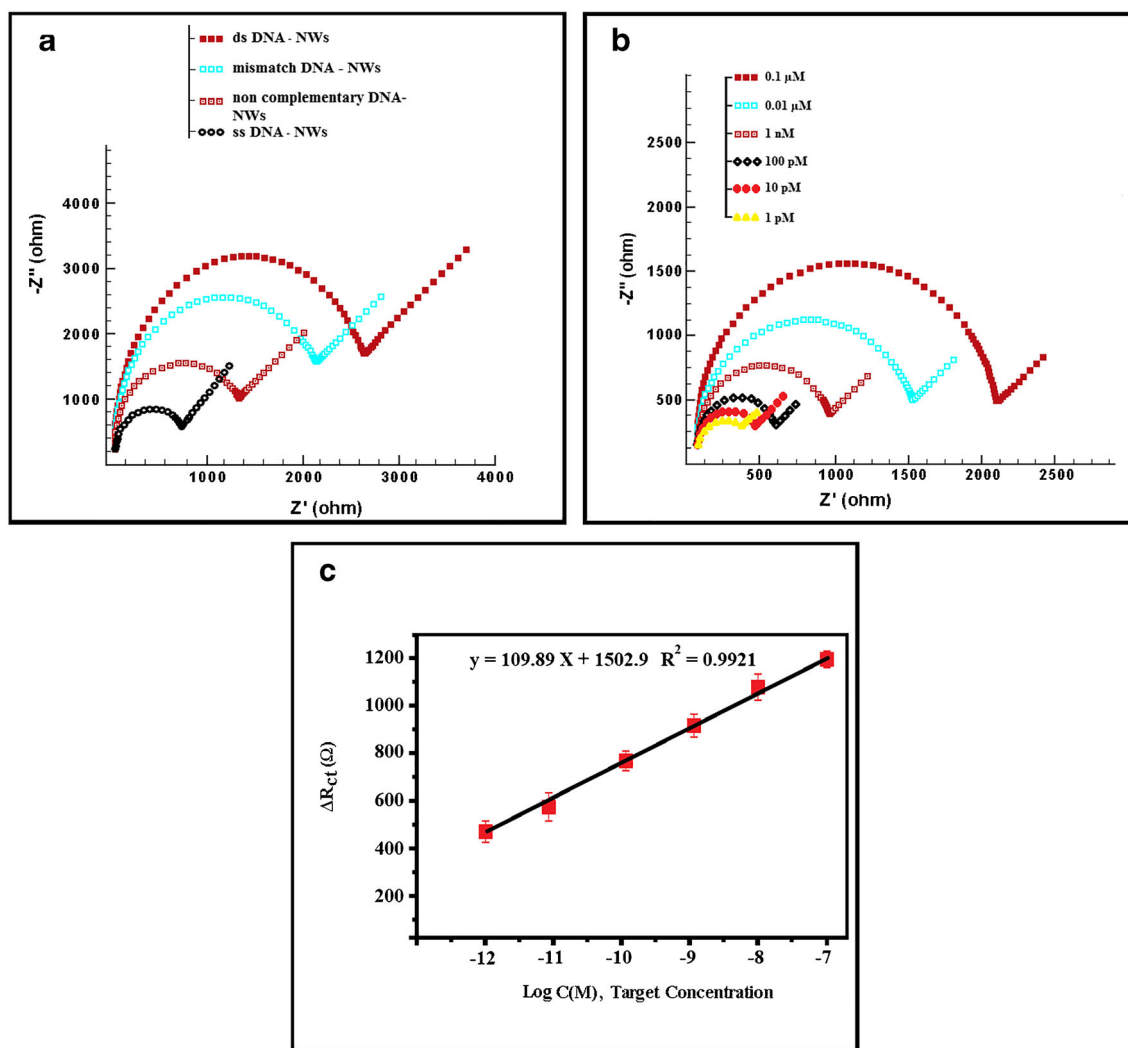


Fig. 6 The EIS spectra of DNA oligonucleotides. **(a)** The mismatch, non-complementary, and complementary target hybridizations measured for the WO_3/ITO NW electrode in $1 \mu\text{M}$ concentration. **(b)** The EIS impedance measurements of the WO_3/ITO NW electrode. The

sensitivity of the biosensor to the complementary sequences measured for WO_3/ITO NWs, from 1 pM to $0.1 \mu\text{M}$. **(c)** The ΔR_{ct} vs. complementary target concentrations ($\log C(M)$)

Due to the high tendency of the thiol group with gold, the thiolated DNA oligonucleotide forms a self-accumulating single layer on the gold surface. The conformational changes during DNA hybridization cause changes in charge transfer resistance (R_{ct}) and limit the transfer of mass in diffusion-controlled region. Normally, as the concentration of electro-active ions increases, the R_{ct} decreases. On the other hand, due to the formation of a more integrated and compressed single layer, the concentration enhancement would lead to an increase in R_{ct} and prevents electro-active species (in this case, ferro/ferrite) from reaching to the electrode surface and create a higher potential barrier for electron transfer. Due to configuration and double-layer thickness changes at the electrode/electrolyte interface in non-complementary and mismatch hybridization, the position and sequencing of the base mismatches in DNA sequences on the electrode surface would effect on the R_{ct} and diffusion [26]. In general, the most

complete configuration belongs to the complementary sequence on the surface of the electrode and any change in base sequencing would lead to R_{ct} and diffusion alters.

The enhancement in R_{ct} is mainly due to the electrostatic repulsion between negatively charged phosphate groups in the DNA backbone and the ferro/ferrite ions in the solution. The electrostatic repulsion prevented the transfer of these ions to the electrode surface and led to a resistance enhancement against the charges' mobility. In addition, the selectivity of the complementary sequence related to the immobilized probe on the electrode surface is also another factor for characterized electrode response. Due to the electrode selectivity and the non-specific interaction of non-complementary and mismatch targets on the electrode surface, the R_{ct} changes in non-complementary or mismatch targets are less than complementary sequences. In fact, the absorption of small amounts of these sequences on the electrode surface can limit the transfer

of ferro/ferrite species to the electrode surface in comparison to the single-stranded DNA electrode.

Sensitivity The sensitivity of the WO₃/ITO NW electrode was investigated by testing the biosensor responses to various concentrations of complementary oligonucleotide targets. The measurements were conducted from 1 pM to 0.1 μM range of concentrations (Fig. 6b). The sensitivity of the WO₃/ITO NW electrode without laser amplification reached to 1 pM. The R_{ct} values were enhanced by increasing the concentration of the complementary DNA target. In Fig. 6b, it is completely obvious that the WO₃/ITO NW electrode showed high sensitivity. The present research in comparison to past ones showed relatively good results. The compared discussion will be reviewed in the following section. Figure 6c indicates the calibration curve for the hybridization of the probe with complementary HBV DNA target in different concentrations. For plotting calibration curve, the ΔR_{ct} values were attained from simulated circuit.

Reproducibility The reproducibility of the WO₃/ITO NW DNA biosensors was measured. The reproducibility of the WO₃/ITO NW DNA electrode was calculated in 1 nM concentration. The relative standard deviation (RSD) values for WO₃/ITO NWs were 5.96, 3.26, and 0.62% for complementary, mismatch, and non-complementary, respectively. The RSD values showed good reproducibility for WO₃/ITO NWs. Due to configuration and double-layer thickness changes at the electrode/electrolyte interface in non-complementary and mismatch hybridization, the position and sequencing of the base mismatches in DNA sequences on the electrode surface would effect on the R_{ct} and diffusion. In fact, some bases in non-complementary and mismatch sequences have not bonded to ssDNA complementary bases and they are thermodynamically and spatially free. So, they have lesser role in EIS responses in comparison to complementary ones. So, the RSD values for non-complementary are close to those for ssDNA.

Stability The stability of the WO₃/ITO NW electrode before laser amplification was checked by storing the biosensors in the freezer at 4 °C for 6 weeks, and the results showed that the maximum response of the WO₃/ITO NW biosensors was able to retain 88% of their initial responses, respectively (see ESM Fig. S2).

The analytical EIS measurements for biosensor after laser amplification

Selectivity The DNA biosensor properties were investigated under laser amplification by exploiting the photogeneration mechanism. Figure 7a shows the selectivity of the WO₃/ITO NW surface with DNA probe, mismatch, non-complementary,

and complementary targets in 1 μM concentration after laser application. Randle's equivalent circuit is pictured in Fig. 7a. The elements in equivalent circuit are the charge transfer resistance (R_{ct}), solution resistance (R_s), and constant phase element (CPE). The Warburg impedance (Z_w) which is in the circuit originates from the mass diffusion at low frequencies [24]. In the Nyquist plot at the lower frequencies, the Warburg impedance (Z_w) element shows the diffusion process in the electrode/electrolyte interface and this element is used to indicate the share of species penetration and diffusion. As can be seen at low frequencies, in fact, this element presents the emptying of the diffusion layer and the expansion of this layer and also shows the need to re-diffuse the ferro/ferrite species from the solution volume to the electrode/electrolyte interface at sufficiently long times. This element is displayed in parallel with the circuit (RCPE), and the reason for this is that before the semicircle part of the Nyquist plot could be completely cut the horizon line, it begins to rise again, indicating that a phenomenon is taking place in parallel with the phenomenon of charge transfer in the electrode/electrolyte interface. Figure 7b shows the selectivity of the WO₃/ITO NW surface with DNA probe, mismatch, non-complementary, and complementary targets in 0.1 pM concentration after laser application.

Sensitivity Figure 7c and d shows the sensitivity and calibration curve of the WO₃/ITO NW electrode after laser amplification by testing the biosensor response to various concentrations of complementary oligonucleotide targets, respectively. The analyses were performed from 0.1 pM to 10 μM ranges of concentrations, and the calibration curve for the WO₃/ITO NW electrode was plotted under the efficacy of laser amplification.

In Fig. 7c for lower concentrations (concentrations lower than 0.1 μM and 10 μM), the Nyquist plots at lower frequencies show the diffusion-controlled domination. In other means, the ferro/ferrite species diffusion into the electrode/electrolyte interface is dominated. In fact, the change in the penetration and diffusion values of the ferro/ferrite species at the lower frequency ranges is the main cause of the Nyquist plots alterations in lower concentrations.

Figure 7d indicates that ΔR_{ct} has a linear relationship with the concentrations (logarithmic) of the complementary DNA sequences in the range from 0.1 pM to 10 μM (Fig. 7d). The results indicated that the maximum response of the biosensor retained 96% of its initial response after 6 weeks. The limit of detection (LOD) of the biosensor was 1 fM. The LOD calculations were performed by $Y = S_b + 3\sigma_b$, where σ_b and S_b are the standard deviation and the signal of the blank, respectively.

Reproducibility The reproducibility of the WO₃/ITO NW electrode under laser amplification was investigated, and the RSD values for WO₃/ITO NWs after laser

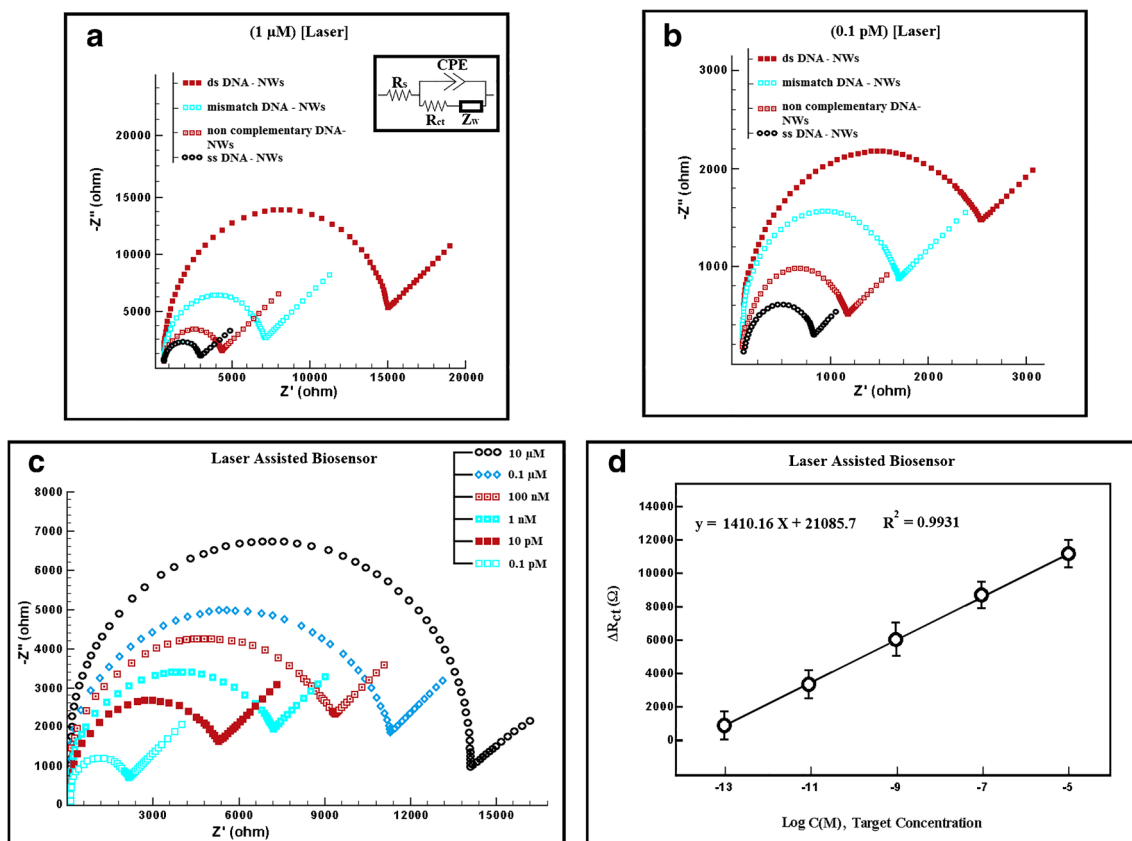


Fig. 7 The EIS spectra of DNA oligonucleotides under laser amplification. The mismatch, non-complementary, and complementary target hybridization measured for the WO₃/ITO NW electrode in 1 μM (a) and 0.1 pM (b) concentrations. (c) The EIS sensitivity measurements

for WO₃/ITO NWs from 0.1 pM to 10 μM. (d) The linear relation between the ΔR_{ct} and the log scale of the concentrations of the complementary DNA sequences in the WO₃/ITO NWs

amplification were 1.67, 1.92, and 2.02% at 1 nM for complementary, mismatch, and non-complementary, respectively.

Stability The stability of the DNA biosensor under laser amplification was evaluated in the freezer at 4 °C after 6 weeks (ESM Fig. S3).

The calculated elements of Randle's circuit for the WO₃/ITO NWs are shown in Tables S1 and S2 in the ESM. The calculated parameters were achieved for the WO₃/ITO NWs with and without laser amplification.

The photocurrent transient response for the WO₃/ITO NW electrode for DNA detection

For exploring the origins of these excellent photoelectrocatalytic properties, a discussion of the interaction between the tin-doped WO₃/In₂O₃ NW heterojunction array and band gap structure is necessary. By applying excitation light to surface of the WO₃/ITO NWs, the possibility of the electron-hole coupling

materialization was realized. In this heterogeneous structure, with the creation of exciton, the light absorption was intensified. In addition, the electrons generated by the laser were transferred from the ITO conduction band (0.1 eV) to the WO₃ conduction band (0.64 eV), and the holes generated by the laser were transferred from the WO₃ valence band (3.54 eV) to the ITO valence band. With the creation of a proper mechanism in the energy gradient (band gap), it was possible to separate the electron-hole couples and increase the efficiency of the photocurrent stability and conversion process. This enhancement in performance was investigated by enhanced light absorption and photocurrent measurements. The stability of tin-doped WO₃/In₂O₃ NW configuration was calculated via photocurrent density percentage in the 5-min intervals, a comparison between last cycle (end) and first cycle (start). In addition, as presented in Fig. 8, the transient photocurrent showed a fast response as soon as the laser was lighted on. For better explanation, electrons in tin-doped WO₃/In₂O₃ NWs would be gathered before the laser switched on, while they would back to zero when

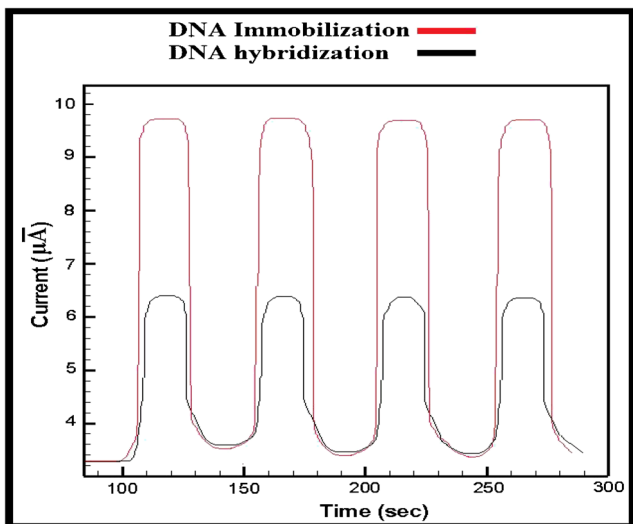


Fig. 8 Transient photocurrent response of the samples at a 60-s light on/off. Black, NW DNA hybridization; red, NW DNA immobilization at 1 µM

the laser was off. This approach indicates that the materialized NWs responded intensively to the laser radiation. Furthermore, there is a determined decay during the illumination time caused by the photogenerated charge carriers which assembled before laser was switched on. Practically, the photo-induced carriers caused by laser were centralized during continuous laser radiation.

The comparative study

The sensitivity response and surface coverage of the HBV DNA biosensor are shown in Fig. 9. Figure 9a shows the sensitivity response of the HBV DNA biosensor before and

after laser amplification. Figure 9a demonstrates the high-sensitivity response under laser amplification. The sensitivity response significantly was enhanced after laser amplification (Fig. 9a). Figure 9b shows the surface coverage (Θ) of the WO₃/ITO NW biosensor measured by previously known formula no. 1

$$\Theta = 1 - \frac{R_0}{R_i} \tag{1}$$

where R_0 is the measured R_{ct} of the probe and R_i is the calculated R_{ct} of the complementary target. Under laser amplification, the surface coverage of the WO₃/ITO NW biosensor for the specific target concentrations shows more surface coverage than without laser related to the low concentrations. The most surface coverage was obtained at 0.1 pM. The WO₃/ITO NW biosensor showed a maximum of 78.1% surface coverage. In other means, the 78.1% of the probe sequences were hybridized with the complementary sequences.

The comparative study of the recently published works and well-done researches on the HBV biosensing according to different methods and mechanism with our works is presented in Table 2. Most of recently presented impedimetric biosensors are adapted to model on label-free approach. The presented biosensor showed a lower LOD in wide linear range and is matched comparatively to the cited biosensors. Because of the high sensitivity of the WO₃/ITO NW surface and laser amplification, the WO₃/ITO NW biosensor could demonstrate the better sensitivity, stability, selectivity, and reproducibility in comparison to the mentioned biosensors in Table 2. In this regard, some sensitive genosensor with long-length sequences associated with amplified technique and method was also introduced.

Fig. 9 The sensitivity response (a) and surface coverage (b)

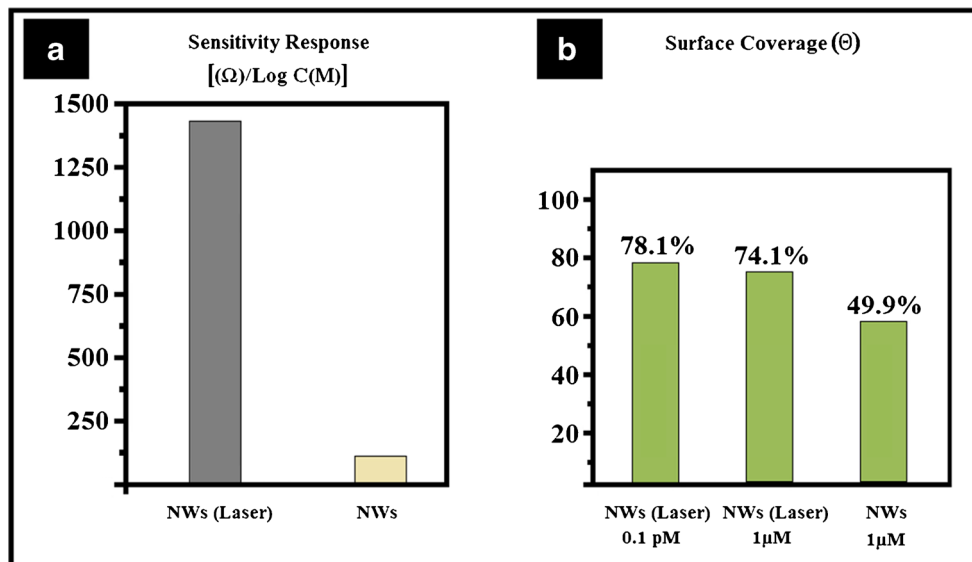


Table 2 Comparison of the previous works on HBV biosensors with the present study

Biosensor	Capture probe (target length)	Limit of detection (LOD)	Linear range	Technique description	Reference
Real-time measurements of DNA hybridization	DNA (16 bp)	10 pM	10 pM–100 nM	PCR	[24]
PNA-DNA hybridization using oxide-etched silicon nanowire	PNA (22 bp)	10 fM	10 fM–1 μ M	SiNW FET	[27]
miRNAs with silicon nanowire FET	PNA (22 bp)	1 fM	1 fM–1 nM	SiNW FET	[28]
Electrochemical/SWV/methylene blue	DNA (10 bp)	0.1 pM	0.1–5 μ M	PCR	[29]
Electrochemical DNA arrays based on silver NPs	DNA (15 bp)	5 aM	10 aM–100 fM	Electrochemical/DPV/PCR	[30]
Carbon nanotube field-effect transistor	DNA (21 bp)	1 pM	1–10 pM	CNT FET	[31]
Carbon nanotube field-effect transistor	DNA (24 bp)	1 pM	1 pM–10 nM	CNT FET	[25]
Graphene/Si nanowire diode type	DNA	0.1 pM	0.1–500 nM	SiNW FET	[9]
Real-time PCR assay for quantitation of HBV DNA	661 nucleotides	10 copies/reaction	10^{10} to 10 copies/reaction	Real-time PCR	[32]
Cobalt oxide porous nanocube-based EIS for HBV DNA in blood serum and urine samples	21 base and blood serum	0.38 pM	0.001–1000 nM	EIS	[33]
Polymerase chain reaction-free detection of hepatitis B virus DNA	103 MER	111 copies/mL	10^2 – 10^3 and 10^3 – 10^5 copies/mL	EIS	[34]
Real-time loop-mediated isothermal amplification for HBV DNA quantification	337 bp	210 copies/mL	8 orders of magnitude	Real-time loop-mediated isothermal amplification (Rf-LAMP)	[35]
WO ₃ /ITO NW photoelectrode	25 bp	1 fM	0.1 pM–10 μ M	EIS	This Work

Conclusion

In conclusion, an ultra-high sensitive HBV DNA biosensor by exploiting the WO₃/ITO NWs under laser amplification has been successfully materialized. The WO₃/ITO NW biosensor under laser amplification could reach to very low LOD in the organized hybridization detection. The fabricated biosensor showed high sensitivity to very low concentrations. Additionally, the biosensor could distinguish the complementary target from the mismatch and non-complementary targets and demonstrated good stability. Therefore, the excellent performance of the materialized DNA biosensor would be very attractive for HBV DNA diagnosis. The photocurrent transient measurements for the WO₃/ITO NW electrode showed that the biosensor under laser illumination had quick and dynamic response.

Compliance with ethical standards

Conflict of interest The authors declare that they have no conflict of interest.

References

- Seo G, Lee G, Kim MJ, Baek SH, Choi M, Ku KB, et al. Rapid detection of COVID-19 causative virus (SARS-CoV-2) in human nasopharyngeal swab specimens using field-effect transistor-based biosensor. *ACS Nano*. 2020;14:5135–42.

- Riahi R, Mach KE, Mohan R, Liao JC, Wong PK. Molecular detection of bacterial pathogens using microparticle enhanced double-stranded DNA probes. *Anal Chem*. 2011;83:6349–54.
- Yang C, Denno ME, JilVenton PP. Recent trends in carbon nanomaterial-based electrochemical sensors for biomolecules: a review. *Anal Chim Acta*. 2015;887(5):17–37.
- Negahdari B, Darvishi M, Asghar SA. Gold nanoparticles and hepatitis B virus. *Artif Cells Nanomed Biotechnol*. 2019;47:469–74.
- Ju H, Zhao H. Electrochemical biosensors for DNA analysis. *Front Biosci*. 2005;10:37–46.
- Wen JK, Zhang XE, Cheng Z, Liu H, Zhou YF, Zhang ZP, et al. A visual DNA chip for simultaneous detection of hepatitis B virus, hepatitis C virus and human immunodeficiency virus type-1. *Biosens Bioelectron*. 2004;19:685–92.
- Escosura-Muiz A, Maltez-da Costa M, Sanchez-Espinel C, Diaaz-Freitas B, Fernandez-Suarez J, Gonzalez-Fernandez AF, et al. Gold nanoparticle-based electrochemical magneto immunosensor for rapid detection of anti-hepatitis B virus antibodies in human serum. *Biosens Bioelectron*. 2009;26:1710–4.
- Caygill RL, Blair GE, Millner PA. A review on viral biosensors to detect human pathogens. *Anal Chim Acta*. 2010;681:8–15.
- Mahdavi M, Samaeian A, Hajmirzaheydarali M, Shahmohammadi M, Mohajerzadeh S, Malboobi MA. Label-free detection of DNA hybridization using a porous poly-Si ion-sensitive field effect transistor. *RSC Adv*. 2014;69:36854–63.
- Mandong G, Yanqing L, Hongxia G, Xiaoqin W, Lifang F. Electrochemical detection of short sequences related to the hepatitis B virus using MB on chitosan-modified CPE. *Bioelectrochemistry*. 2007;70:245–9.
- Tsitsilonis OE, Thrasyvoulides A, Balafas A, Voutsas JF, Papamichail M, Lymberi P. Serological detection of hepatitis B viral infection by a panel of solid-phase enzyme-linked. *J Pharm Biomed Anal*. 2004;34(4):811–22.

12. Urrego LF, Lopez DI, Ramirez KA, Ramirez C, Osma JF. Biomicrosystem design and fabrication for the human papilloma virus 16 detection. *Sensors Actuators B Chem.* 2015;207:97–104.
13. Kang B, Yeo U, Yoo KH. Anodized aluminum oxide-based capacitance sensors for the direct detection of DNA hybridization. *Biosens Bioelectron.* 2010;25:1592–6.
14. Adiga SP, Jin C, Curtiss LA, Monteiro-Riviere NA, Narayan RJ. Nanoporous membranes for medical and biological applications. *Wiley Interdiscip Rev Nanomed Nanobiotechnol.* 2009;1:568–81.
15. Seidenstücker A, Beirle S, Enderle F, Ziemann P, Marti O, Plettl A. Nanoporous silicon nitride-based membranes of controlled pore size, shape and areal density: Fabrication as well as electrophoretic and molecular filtering characterization. *Beilstein J Nanotechnol.* 2018;9:1390–8.
16. Escosura-Muniz A, Merkoci A. Nanochannels preparation and application in biosensing. *ACS Nano.* 2012;6:7556–83.
17. Stroeve P, Ileri N. Biotechnical and other applications of nanoporous membranes. *Trends Biotechnol.* 2011;29:259–66.
18. Juhasz L, Mizsei J. Humidity sensor structures with thin film porous alumina for on-chip integration. *Thin Solid Films.* 2009;517:6198–201.
19. Steinmetz M, Lima D, Gonçalves A, Sérgio V, Fujiwara T, Andrade Pessôa C, et al. A sensitive label-free impedimetric DNA biosensor based on silsesquioxane-functionalized gold nanoparticles for Zika virus detection. *Biosens Bioelectron.* 2019;141:111351.
20. Ye WW, Shi JY, Chan CY, Zhang Y, Yang M. A nanoporous membrane based impedance sensing platform for DNA sensing with gold nanoparticle amplification. *Sensors Actuators B Chem.* 2014;31:877–82.
21. Said S, Mikhail S, Riad M. Recent progress in preparations and applications of meso-porous alumina. *Mater Sci Energy Technol.* 2019;2:288–97.
22. Zhang J, Ma H, Liu Z. Highly efficient photocatalyst based on all oxides WO₃/Cu₂O heterojunction for photoelectrochemical water splitting. *Appl Catal B Environ.* 2017;201:84–91.
23. Shariati M. The continuous and persistent periodical growth induced by substrate accommodation in In₂O₃ nanostructure chains and their photoluminescence properties. *Appl Phys A.* 2015;118:997–1007.
24. Bunimovich YL, Shin YS, Yeo WS, Amori M, Kwong G, Heath JR. Quantitative real-time measurements of DNA hybridization with alkylated nonoxidized silicon nanowires in electrolyte solution. *J Am Chem Soc.* 2006;128:16323–31.
25. Shariati M. The field effect transistor DNA biosensor based on ITO nanowires in label-free hepatitis B virus detecting compatible with CMOS technology. *Biosens Bioelectron.* 2018;105:58–64.
26. Takmakov P, Vlassiok I, Smirnov S. Hydrothermally shrunk alumina nanopores and their application to DNA sensing. *Analyst.* 2006;131:1248–53.
27. Zhang G, Chua J, Chee R, Agarwal A, Wong S, Buddharaju K, et al. Highly sensitive measurements of PNA-DNA hybridization using oxide-etched silicon nanowire biosensors. *Biosens Bioelectron.* 2009;23:1701–7.
28. Tran TT, Mulchandani A. Carbon nanotubes and graphene nano field-effect transistor-based biosensors. *TrAC Trends Anal Chem.* 2016;79:222–32.
29. Ahangar LE, Mehrgardi MA. Amplified detection of hepatitis B virus using an electrochemical DNA biosensor on a nanoporous gold platform. *Bioelectrochemistry.* 2017;117:83–8.
30. Li H, Sun Z, Zhong W, Hao N, Xu D, Chen HY. Ultrasensitive electrochemical detection for DNA arrays based on silver nanoparticle aggregates. *Anal Chem.* 2010;82:5477–83.
31. Xuan C, Thuy NT, Luyen TT, Huyen TT, Tuan MA. Carbon nanotube field-effect transistor for DNA sensing. *J Electron Mater.* 2017;46:3507–11.
32. Paraskevis D, Haida C, Tassopoulos N, Raptopoulou M, Tsantoulas D, Papachristou H, et al. Development and assessment of a novel real-time PCR assay for quantitation of HBV DNA. *J Virol Methods.* 2002;103:201–12.
33. Kannan P, Subramanian P, Maiyalagan T, Jiang Z. Cobalt oxide porous nanocubes-based electrochemical immunobiosensing of hepatitis B virus DNA in blood serum and urine samples. *Anal Chem.* 2019;91:5824–33.
34. Chen CC, Lai ZL, Wang GJ, Wu CY. Polymerase chain reaction-free detection of hepatitis B virus DNA using a nanostructured impedance biosensor. *Biosens Bioelectron.* 2016;15(77):603–8.
35. Cai T, Lou GQ, Jin Y, Dai X, Meng ZH. Development and evaluation of real-time loop-mediated isothermal amplification for hepatitis B virus DNA quantification: a new tool for HBV management. *J Clin Virol.* 2008;4:270–6.

Publisher's note Springer Nature remains neutral with regard to jurisdictional claims in published maps and institutional affiliations.